

Non-equilibrium critical scaling and universality in a quantum simulator

Received: 22 April 2025

Accepted: 12 August 2025

Published online: 26 August 2025



Arinjoy De^{1,7,9}✉, Patrick Cook^{1,2,3,9}, Mostafa Ali², Kate Collins¹, William Morong^{1,8}, Daniel Paz², Paraj Titum^{1,4}, Guido Pagano⁵, Alexey V. Gorshkov¹, Mohammad Maghrebi² & Christopher Monroe^{1,6}

Universality and scaling laws are hallmarks of equilibrium phase transitions and critical phenomena. However, extending these concepts to non-equilibrium systems is an outstanding challenge. Despite recent progress in the study of dynamical phases, the universality classes and scaling laws for non-equilibrium phenomena are far less understood than those in equilibrium. In this work, using a trapped-ion quantum simulator with single-spin resolution, we investigate the non-equilibrium nature of critical fluctuations following a quantum quench to the critical point. We probe the scaling of spin fluctuations after a series of quenches to the critical Hamiltonian of a long-range Ising model. With systems of up to 50 spins, we show that the amplitude and timescale of the post-quench fluctuations scale with system size with distinct universal critical exponents, depending on the quench protocol. While a generic quench can lead to thermal critical behavior, we find that a second quench from one critical state to another (i.e. a double quench) results in a new universal non-equilibrium behavior, identified by a set of critical exponents distinct from their equilibrium counterparts. Our results demonstrate the ability of quantum simulators to explore universal scaling beyond equilibrium.

In recent years, substantial theoretical^{1–4} and experimental^{5,6} progress has been achieved in understanding emergent behavior of isolated quantum systems out of equilibrium. In this context, non-equilibrium many-body systems can be investigated by measuring quantum dynamics after a quench⁷, namely after a change of the Hamiltonian parameters that is much faster than the typical energy scales in the system—which is routinely performed in AMO (atomic, molecular, and optical) systems.

Although quench dynamics are extremely complex in general, one would expect that macroscopic observables, after a short time, become insensitive to the microscopic details⁸. In particular, in the vicinity of a phase transition, the dynamics should give rise to universal

critical behavior which leads to scale-invariant spatio-temporal correlations with universal exponents⁹. Notably, we show that non-equilibrium critical phenomena can emerge in the context of quench dynamics in one-dimensional systems with long-range interactions. In general, universal non-equilibrium phenomena are relevant far beyond the scope of AMO and condensed matter physics, including chemistry, biology, and even sociology¹⁰. Examples ranging from glassy transitions seen in polymers, colloidal gels, and spin glasses¹¹ to symmetry-breaking transitions in the Universe after the ‘Big Bang’¹² all exhibit non-equilibrium critical behavior.

The unprecedented degree of control over quantum systems in platforms such as trapped ions^{13,14}, ultracold atoms^{15,16}, nitrogen-

¹Joint Quantum Institute and Joint Center for Quantum Information and Computer Science, NIST and University of Maryland, College Park, MD, USA.

²Department of Physics and Astronomy, Michigan State University, East Lansing, MI, USA. ³Facility for Rare Isotope Beams, East Lansing, MI, USA. ⁴Johns Hopkins University Applied Physics Laboratory, Laurel, MD, USA. ⁵Department of Physics and Astronomy, Rice University, Houston, TX, USA. ⁶Duke Quantum Center, Departments of Electrical and Computer Engineering and Physics, Duke University, Durham, NC, USA. ⁷Present address: QuEra Computing Inc., Boston, MA, USA. ⁸Present address: AWS Center for Quantum Computing, Pasadena, CA, USA. ⁹These authors contributed equally: Arinjoy De, Patrick Cook.

✉ e-mail: arinjoy@umd.edu

vacancy centers¹⁷, superconducting circuits^{18,19} and others^{20–22} has made it possible to probe fundamental questions about non-equilibrium many-body physics including prethermalization^{23,24}, many-body localization^{25,26}, discrete time crystals^{17,27}, and dynamical phase transitions^{5,6}. For example, universal scaling around non-thermal fixed points has been observed with Bose-Einstein condensates that exhibit self-similar behavior; these observations are however, not related to an underlying critical behavior^{28–32}. In contrast, the work reported here is fundamentally tied to the existence of a phase transition and extends the remarkably rich domain of critical phenomena in equilibrium to far-from-equilibrium dynamics.

In this work, we investigate the critical behavior in the vicinity of a dynamical phase transition in quench dynamics. An immediate challenge is that a quantum quench generically leads to thermalization³³, thus the resulting critical behavior is effectively thermal^{34,35}. While this is the case in a quench from a gapped initial state, a quench from a gapless state (e.g., the critical point of the Hamiltonian) could lead to genuinely non-thermal critical behavior^{9,36–38} (see the schematic picture in Fig. 1a). We attribute these features to the behavior of the *soft mode*³⁵. Specifically, we find that a generic quench from a gapped initial state excites this mode and heats it up, resulting in effective thermal behavior. In contrast, a critical-to-critical quench leads to *overheating* of the *soft mode*, giving rise to novel non-equilibrium critical behavior.

Results

We probe the post-quench dynamics of a transverse-field Ising chain with tunable power-law interactions. The Hamiltonian of the model is

represented as ($\hbar = 1$):

$$H = - \sum_{i < j}^N J_{ij} (\gamma^x \sigma_i^x \sigma_j^x + \gamma^y \sigma_i^y \sigma_j^y) + B^z \sum_i \sigma_i^z, \quad (1)$$

where $\sigma_i^{x,y,z}$ are the Pauli matrices acting on the i 'th spin. J_{ij} is the interaction strength between ions i and j , B^z is the global transverse magnetic field and N is the number of spins. The coefficients $(\gamma^x, \gamma^y) \in [0, 1]$, and only one of them is non-zero during a single quench (Methods). The interaction strength falls off approximately following a power-law of the form $J_{ij} \sim J/|i-j|^p$, where $J > 0$ is the effective interaction strength and p represents the range of interaction¹³. The exponent p was tuned to be at 0.89 for all the experiments and all system sizes (Methods). We note that, for large system sizes, the interaction matrix elements deviate from a simple power-law behavior and exhibit faster decay at longer distances (see Supplementary Information (SI), Sec. VII.B). In order to maintain a well-defined thermodynamic limit, here onwards, we refer to the interaction after it is Kac-normalized as $\mathcal{J} = \frac{1}{N-1} \sum_{i,j} J_{ij}$ ³⁹. We encode the quantum spins in the ground state hyperfine manifold of the $^{171}\text{Yb}^+$ ions, where $|\downarrow\rangle_z \equiv |^2S_{1/2}, F=0, m_F=0\rangle$ and $|\uparrow\rangle_z \equiv |^2S_{1/2}, F=1, m_F=0\rangle$, and we perform high-fidelity state preparation and site-resolved detection using state-dependent fluorescence (Methods)⁴⁰.

The transverse-field Ising model exhibits a ground-state phase transition from a disordered paramagnet to a magnetically ordered state. As the ratio of Kac-normalized effective interaction field ($\mathcal{J}\gamma^x$) to the transverse magnetic field (B^z) is varied across the critical point $\mathcal{J}\gamma^x/B^z = 1$, the average in-plane magnetization ($\langle\sigma^x\rangle$) changes from zero (disordered phase) to a non-zero value (ordered phase) in a

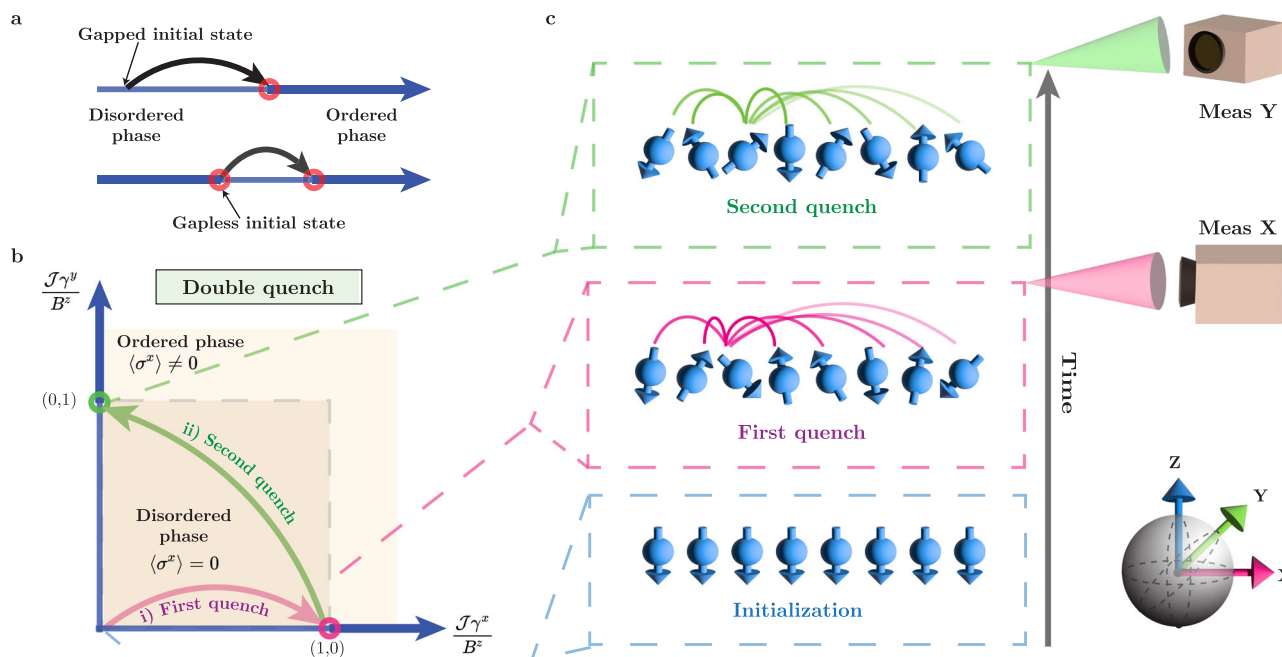


Fig. 1 | Critical quench dynamics. **a** Disorder-to-order phase transitions emerge even in the non-equilibrium setting of quench dynamics, and exhibit critical behavior at the transition. The ordered and disordered phases are shown in thick and thin lines, respectively, and the arrows indicate a quench to the critical point. While a quench from a gapped initial state (top panel) to the critical point (red circles) generically leads to effective thermal behavior, a quench from a gapless state (bottom panel), corresponding to a distinct critical point, gives rise to non-equilibrium criticality. **b** Ground-state phase diagram with Ising interaction along x or y direction. $\mathcal{J}\gamma^{x,y}/B^z$ is the ratio of the Kac-normalized effective interaction strength $\mathcal{J}\gamma^{x,y}$ to the transverse field strength B^z (see text). The phase boundary is

shown in gray dashed lines, with red and green circles indicating the critical points where the quenches are performed. **c** The experimental sequence starting with all spins initialized along $|\downarrow\rangle_z$. The first quench is applied with interactions along the x direction, and the evolution is measured by projecting the spins along x . For the second quench, both the interaction and measurement bases are switched from x to y direction. In the double-quench experiment, the second quench is applied after evolving under the first quench, but no measurement is performed before the second quench. The curved lines illustrate the long-range interaction among all the spins where the opacity reflects interaction strengths that weaken with distance.

second-order phase transition (Fig. 1a). By performing quenches to various values of $\mathcal{J}B^z/B^z$, we identify the critical point of this phase transition and observe the characteristic divergent fluctuations. We report that, after a single quench from a gapped initial state, the critical behavior and exponents are effectively thermal; see Fig. 1a (top panel). In contrast, the scenario in Fig. 1a (bottom panel) involves preparing a critical initial state, which is experimentally challenging. Instead, we show that a sequence of quenches to multiple critical points (Fig. 1b) achieves the same objective and leads to non-equilibrium critical behavior.

We begin with a single quench sequence where all the spins are initialized in the $|\downarrow\downarrow\cdots\downarrow\rangle_z$ state, which is the gapped ground state of the initial Hamiltonian in the absence of the Ising interaction (SI Sec. III). Then the spin system is evolved after an interaction quench of the form Eq. (1), in which $\gamma^x = 1$, $\gamma^y = 0$ (Fig. 1a). We measure the total spin $S_x = \sum_i^N \sigma_i^x/2$ projected along the direction of interaction (here along x) and calculate the net correlator defined as

$$\langle C_x^2 \rangle = \langle S_x^2 \rangle - \langle S_x \rangle^2. \quad (2)$$

We characterize the dynamics through the net correlator since the Ising symmetry of the Hamiltonian and the initial state implies that the average magnetization along the x direction remains zero at all times. The definition of $\langle C_x^2 \rangle$ further removes any bias of the average magnetization due to imperfect single-qubit rotations in the experiment. In the Supplementary Fig. 1, we report the post-quench evolution of $\langle C_x^2 \rangle/N^2$ with 10 ions. The observed net correlator increases in amplitude and exhibits slower dynamics as B^z is swept from larger to smaller values, consistent with numerical simulation that includes the decoherence effects of the experiment. This behavior hints at a continuous dynamical phase transition³.

Equilibrium phase transitions are commonly identified by defining an order parameter that acquires a nonzero value as the system transitions from the disordered to the ordered phase. Analogous to equilibrium phases, one may consider the in-plane magnetization to identify a dynamical phase transition. Using a mean-field analysis to compute the long-time average of the magnetization, we can identify $B_c^z/\mathcal{J} = 1$ as the dynamical critical point of the disorder-to-order phase transition, which coincides with the ground-state critical point (SI Secs. III & V). While magnetization remains zero for our chosen initial state, we instead consider the temporal maximum of the net correlator, $\mathcal{M}^2 = \max_t [\langle C_x^2 \rangle/N^2]$, as a proxy for the order parameter; the maximum is chosen to find a large signal in spite of decoherence.

In Fig. 2, we show \mathcal{M}^2 as a function of the scaled magnetic field strength B^z/\mathcal{J} . While there is no sharp transition for finite system sizes ($N = 10, 15, 20$), the order parameter clearly shows an inflection point around $B^z/\mathcal{J} \sim 1$ and a peak at small B^z , indicating the onset of ordering. Notably, the observed order parameter qualitatively follows the mean-field prediction in the ordered phase, $\mathcal{M}^2 \propto (B^z/\mathcal{J})(1 - B^z/\mathcal{J})$; see the dashed line in Fig. 2. Moreover, one can even capture the finite-size corrections by considering fluctuations at finite system sizes. The solid lines in Fig. 2 depict the function describing the finite-size corrected order parameter, which has the critical point and an overall scale as fit parameters. The inferred critical values are well in agreement with the mean-field prediction (SI Secs. IV.A & IV.C). Having identified the dynamical critical point, the immediate questions are: What is the nature of the critical behavior at the phase transition, and does it genuinely go beyond the equilibrium paradigm?

As a first step toward answering these questions, we experimentally scale up the single quench experiment to system sizes up to $N = 50$ ions and observe the net correlator which, at the critical point, characterizes critical fluctuations. As we calibrate the quench Hamiltonian parameters to be at the (mean-field) critical point for all the system sizes, within our experimental uncertainty, we see that the fluctuations

grow and evolve more slowly with increasing system size, indicating an emergent universal critical behavior (Fig. 3a). We identify similar behavior by a numerical simulation of the quench dynamics with experimental spin-spin coupling parameters for system sizes up to $N = 25$ (Supplementary Fig. 3), the maximum number of spins that can be simulated using available computational resources. Such critical behavior leads to scaling relations which are independent of microscopic length/time scales⁴¹. Using scaling analysis, we find the net correlator satisfies the functional form given by⁹

$$\langle C_x^2 \rangle = N^{1+\alpha_1} f\left(\frac{\mathcal{J}t_1}{N^{\zeta_1}}\right), \quad (3)$$

where the exponent α_1 characterizes the amplitude scaling of fluctuations with system size and ζ_1 describes the dynamical scaling. We verify that the scaling relation and the experimentally-obtained exponents $\alpha_1 = 0.42$ (14), and $\zeta_1 = 0.19$ (8) (see Fig. 3b), are consistent with the results of the exact simulation (see Supplementary Fig. 3). The procedure to determine exponents that yield the best collapse of the data is detailed in the SI Sec. VIII. Remarkably, the above exponents are also consistent with mean-field exponents at the thermal phase transition⁹ $\alpha_1 = 1/2$, $\zeta_1 = 1/4$ (SI Sec. IV.B). Additionally, we fit the maximum amplitude of fluctuations against N^{α_1} to obtain the exponent $\alpha_1 = 0.50(4)$ (see the inset of Fig. 3b) which is in excellent agreement with that of thermal equilibrium. Indeed, it is expected that the latter procedure leads to a more precise exponent α_1 since the dynamical features are more susceptible to decoherence. Note that the numerically obtained exponents do not account for decoherence due to the limitations of numerical methods for the system sizes considered here (Methods).

An effective thermal critical behavior is to be expected in quench dynamics if a phase transition exists^{34,35}, but this typically requires higher dimensions or, in this case, long-range interactions. The emergence of the thermal critical exponents does not mean that the system has thermalized. In fact, long-range interacting systems often exhibit prethermalization for a long window in time^{24,42,43}. Instead, the thermal exponents should be attributed to the effective thermalization of the soft mode³⁵. This can be understood through a Holstein-Primakoff transformation that maps spins to bosonic variables, $\sigma_i^\pm \rightarrow \frac{1}{\sqrt{N}}(a_i \pm a_i^\dagger)$, a mapping that is valid near a fully polarized state along the z direction. The lowest energy excitation of the system corresponds to a collective excitation of a bosonic mode, characterized by the operator $a \equiv \sum_i a_i$, which becomes gapless (*softens*) at the phase transition. The total spin can be then described as $S_x \rightarrow \sqrt{N}x$ where $x \sim a + a^\dagger$ may be interpreted as the position operator of a harmonic oscillator with a characteristic frequency Ω which vanishes at the phase transition. Applying the equipartition theorem, $\lim_{t \rightarrow \infty} \Omega^2 \langle x^2 \rangle_t \sim T_{\text{eff}}$ at long times, we find that the gapless mode is described by a finite effective temperature (SI Secs. IV.A & V.A). In fact, identifying $\langle x^2 \rangle \sim N^\alpha$ and $\Omega \sim N^\zeta$, the equipartition theorem reveals that the effective temperature obeys the scaling relation $T_{\text{eff}} \sim N^{\alpha-2\zeta}$. Now, with $\alpha \rightarrow \alpha_1 = 1/2$ and $\zeta \rightarrow \zeta_1 = 1/4$, the effective temperature becomes a constant independent of system size, consistent with thermal equilibrium behavior. Finally, we note that while the description of the soft mode in terms of the spin operators takes a more complicated form due to the experimental interaction matrix, our scaling analysis remains valid (see SI Secs. V & VI).

To break away from the effective thermalization, we now consider the scenario in Fig. 1a. (bottom panel) where the initial state is gapless (i.e., critical) itself. However, realizing such a scheme in experiment can be challenging as it requires high-fidelity adiabatic preparation of the non-trivial critical state prior to the quench. In this work, we instead modify this scheme by applying a sequence of critical quenches. While the resulting critical behavior from multiple quenches is not quantum in nature, due to the over-heating of the soft mode, the

prethermalization of our quantum system is crucial to evade thermalization and hence identify genuinely non-equilibrium behavior⁴⁴.

Experimentally, we first perform a single quench ($\gamma^x = 1, \gamma^y = 0$) to a critical point and evolve until the fluctuations reach their first maxima. Then we switch the interaction from the x to the y -direction (Fig. 1c) to apply a second quench, i.e. we make $\gamma^x = 0, \gamma^y = 1$ (Methods). The intermediate evolution after the single quench brings the system to a critical state when the second quench is applied. Upon the second quench, the dominant fluctuations form along the y -direction and in Fig. 4a, we show the unscaled fluctuations ($\langle C_y^2 \rangle / N$) for system sizes up to 50 ions. These fluctuations also obey the scaling relation in Eq. (3), but with the replacement $C_x^2 \rightarrow C_y^2, t_1 \rightarrow t_2$ (time after the latest quench)

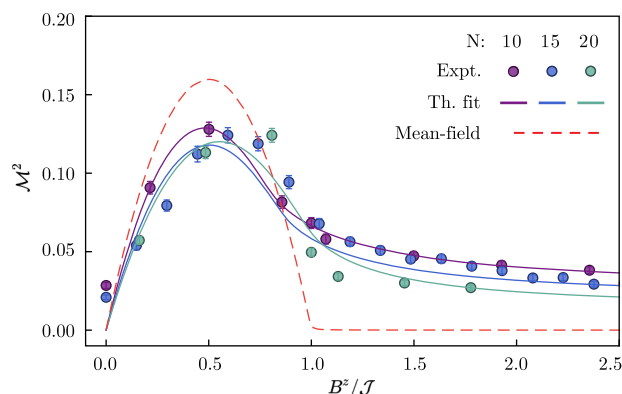


Fig. 2 | Phase transition from order parameter. We report scaled maximum net correlator $\mathcal{M}^2 = \max_t[\langle C_x^2 \rangle / N^2]$ as a function of B^z/J for system sizes $N = 10, 15, 20$. The solid lines are obtained by fitting the experimental data to the finite size corrected order parameter (Eq. (28) of SI), which has the critical point as a fit parameter. The extracted values are 0.83 (19), 0.88 (6), 1.01 (9), respectively for $N = 10, 15, 20$; the difference from the predicted critical point $B^z/J = 1$ is due to finite-size effects and experimental imperfections. For simplicity, we use the predicted critical value for studies in Figs. 3, 4. The dashed line represents the mean-field solution with an inflection point at $B^z/J = 1$. For the comparison of the experimental data against decoherence-free numerical simulation, see Supplementary Fig. 2. The error bars are statistical fluctuations around the mean value.

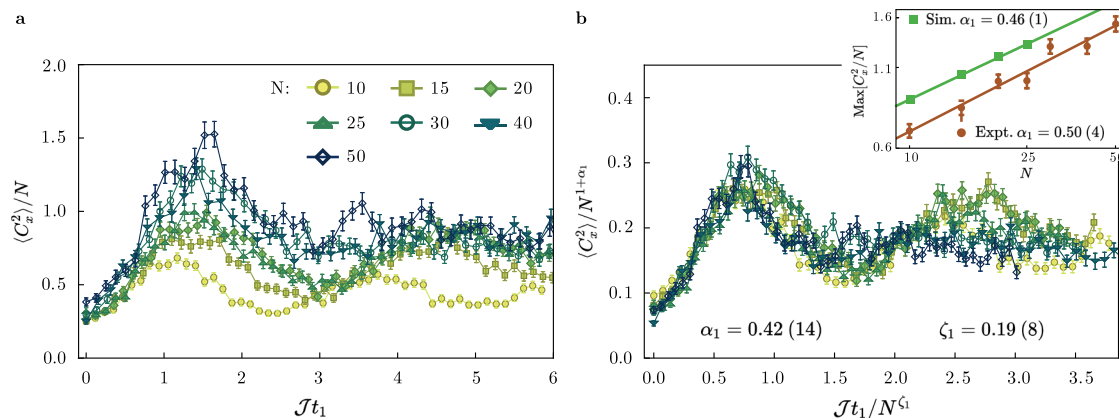


Fig. 3 | Unscaled (a) and scaled (b) fluctuations after a single quench. a We report experimental critical fluctuations with system sizes up to $N = 50$ ions. We obtain the critical scaling exponents (α_1, ζ_1) by optimizing the weighted Euclidean distance between each of the curves to get the best collapse for the experimental (b) data [see main text for details]. We observe remarkable similarity between the exponents found in the experiment and simulations (see Supplementary Fig. 3), highlighting the universality of the exponents despite experimental imperfections as well as finite-size effects. Comparing the decoherence-free numerical simulation in Supplementary Fig. 3 with the experimental data, we note that the fluctuations in the experiment are reduced due to decoherence and imperfect detection fidelity;

and with a new set of exponents α_2 and ζ_2 identifying a new universal critical behavior. We find the optimal collapse for $\alpha_2 = 0.63(33)$ and $\zeta_2 = 0.10(17)$ (Fig. 4b). We verify that exact numerical simulation results in very similar critical exponents (Supplementary Fig. 4). Notably, these exponents are also in good agreement with the analytical values $\alpha_2 = 3/4$ and $\zeta_2 = 1/8$ obtained for the infinite-range LMG model (see SI Sec. IV.D), underscoring the universal character of the observed critical behavior. Finally, we remark that the effective temperature now scales as $T_{\text{eff}} \sim N^{\alpha_2 - 2\zeta_2}$, which shows a nontrivial scaling with system size, underscoring a dramatic departure from equilibrium critical behavior. Such non-equilibrium criticality generally emerges upon a quench from a gapless state, and can be attributed to the over-heating of the soft mode^{9,36–38} (see SI Sec. IV).

Experimental decoherence causes the observed fluctuations to be damped for both single and double quenches. We see that the unscaled 50 ion fluctuations after the double quench are significantly damped (Fig. 3a). The major sources of decoherence, which scale with the system size, remain within acceptable thresholds for system sizes $N < 50$, but these errors start to dominate for $N \geq 50$ (“Methods”). This effect is more adverse for the double-quench sequence than the single-quench, since the former involves longer evolution under two quenches. For completeness, we have included all the 50 ion data in Fig. 4a, c, but excluded it in determining the best collapse exponent. Fitting the maximum amplitudes of the fluctuations to N^{α_2} yields exponent $\alpha_2 = 0.69(9)$, with tighter error bounds (Inset Fig. 4c). Errors in identifying the peak fluctuation result in erroneous switch time between the two quenches, contributing to imperfect exponents. This effect can be reproduced in the simulation with exact experimental parameters, and correction for such errors in further simulations results in exponents that are well in agreement with the analytically predicted non-equilibrium values (SI Sec. VII.D).

Discussion

In this work, we have demonstrated the ability to identify, both numerically and experimentally, the dynamical critical point of a disorder-to-order phase transition in a 1D transverse-field Ising model. We have observed the non-equilibrium critical behavior upon single and double quenches with up to 50 ions and extracted the universal scaling exponents, which agree with the predictions of numerical

however, as we can see from the scaled data, the scaling collapse is still observed for all the system sizes. In the inset b, we find consistent scaling exponents by fitting the maximum values of the fluctuation (dots) to a power-law fit to N^{α_1} (solid lines). Although this method does not capture the full evolution, we get excellent agreement of exponents for both the simulation and the experiment. The data points from numerical simulation (in green) do not account for decoherence, resulting in higher peak values as compared to the experimental values (see Supplementary Fig. 3). In Supplementary Fig. 3b, we present numerical simulations of critical dynamics for $N = 10$ and 15, incorporating decoherence effects. The error bars of the experimental data are statistical fluctuations around the mean value.

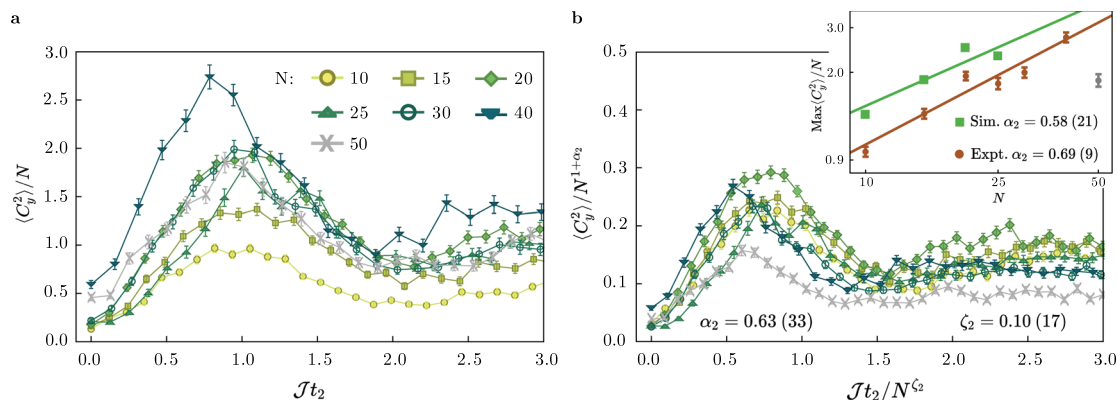


Fig. 4 | Unscaled (a) and scaled (b) fluctuations after a double quench. **a** We plot the unscaled fluctuations along y direction at the predicted critical points for system sizes of $N = 10$ –50 ions. The second quench is applied when the fluctuations following the first quench reach their maxima and the time t_2 is counted after the second quench. **b** We apply the same scaling collapse technique as for the single quench to find the best scaling exponents (α_2 , ζ_2) for the experimental data. See Supplementary Fig. 4 for numerical simulations of the data. We observe that the critical fluctuations do not monotonically grow for increasing system sizes, as

simulation of up to 25 spins. A high level of experimental control was achieved by realizing self-similar interaction matrices across different system sizes, which is essential for experimentally identifying and characterizing the critical points of a phase transition. While the decay of experimental spin-spin interactions deviates from the exact power-law models with $p < 1$ (see SI Sec. VII.B), the resulting universal critical behavior follows the latter models closely, a feature that is also reflected in the spin-spin correlation function (see SI Sec. VII.C). Furthermore, we theoretically predict that the observed double-quench critical scaling is only the first in an infinite hierarchy of universal critical behaviors that emerge in a sequence of multiple quenches (SI Sec. IV.D), an exciting direction to investigate in the future. Future work could also explore extensions of our spin-based trapped-ion simulator to non-equilibrium dynamics that include other degrees of freedom, such as phonons⁴⁵.

Methods

State preparation and readout

The quantum simulator used in this experiment is based on $^{171}\text{Yb}^+$ ions trapped in all three directions in a 3-layer Paul trap⁴⁶ with transverse center of mass (COM) mode frequencies ranging from $\nu_{\text{COM}} = (4.64$ – $4.73)$ MHz and axial COM mode frequencies ranging from $\nu_x = (0.23$ – $0.53)$ MHz depending on system size ($N = 10$ – 50), with axial frequency being lowered to accommodate more ions in a linear chain. Before each experimental cycle, the ions are Doppler cooled in all three directions by a 369.5 nm laser beam, 10 MHz red-detuned from the $^2S_{1/2}$ to $^2P_{1/2}$ transition. We use the same laser to optically pump all the ions to initialize them in the low-energy hyperfine qubit state, $|\downarrow_z\rangle \equiv ^2S_{1/2}|F=0, m_F=0\rangle$ with $>99\%$ fidelity. In addition to Doppler cooling, we apply the resolved sideband cooling method to bring the ions to their motional ground state with $>90\%$ fidelity. After the Hamiltonian evolution, we apply global $\pi/2$ rotations using composite BB1 pulses to project the spin along the x or y direction of the Bloch sphere from the z direction. We then measure the magnetization of each spin using a state-dependent fluorescence by applying a beam resonant with the $^2S_{1/2}|F=1\rangle \leftrightarrow ^2F_{1/2}|F=0\rangle$ transition. The ions scatter photons if they are projected in the $|\uparrow_z\rangle$ state, and appear bright, while in $|\downarrow_z\rangle$ state, the number of scattered photons is negligible and the ions appear dark. A finite-conjugate NA = 0.4 objective lens system (total magnification of 70 \times) collects scattered 369.5 nm photons and

would be expected from the scaling relations. This effect can be attributed to the imperfect switching time between the first and second quench; a nearly perfect collapse can be reproduced numerically using the precise switch times (SI Sec. VII.D). We also report exponents found by a power-law fit of the maximum fluctuations which agree more closely with the analytical prediction (Inset b.). While determining the experimental critical exponents, we have excluded 50 ion data (gray) [see main text for details]. The error bars of the experimental data are statistical fluctuation around the mean value.

images them onto an EMCCD camera, which allows us to perform site-resolved magnetization and correlation measurements with average fidelity of 97%. No state preparation and measurement (SPAM) correction has been applied to data presented in this work. More details of this experimental apparatus can be found in our previous works^{13,27,47}.

Generating XX and YY type Ising interaction

The global spin-spin interaction in the trapped ion system in consideration is generated by applying a spin-dependent force via non-copropagating 355 nm pulsed laser beams that uniformly illuminate the ion chain. The pair of beams has a relative wavevector difference along the transverse motional direction of the ions. These beams are controlled by acousto-optic modulators which impart beatnote frequencies at $\nu_{\text{COM}} \pm \mu$, and phases (ϕ_b, ϕ_r) , respectively, where μ is the symmetric detuning from the COM mode (≈ 56 kHz). These two tones respectively drive the blue (BSB) and red (RSB) sideband transitions, which, following the Mølmer-Sørensen (MS) protocol⁴⁸, generate an effective Hamiltonian

$$H = \sum_{i=1}^N \sum_{m=1}^N \frac{\eta_{i,m} \Omega_i}{2} \left[a_m e^{i\delta_m t} e^{i\phi_M} + a_m^\dagger e^{-i\delta_m t} e^{-i\phi_M} \right] \sigma_i^{\phi_s}, \quad (4)$$

where $\eta_{i,m}$ is the Lamb-Dicke parameter for ion i and mode m , Ω_i is the Rabi frequency at ion i , a_m^\dagger, a_m are the creation and annihilation operators of motional quanta for m th motional mode, $\delta_m = \mu - \nu_m$ is the MS detuning from the m th motional mode frequency ν_m . $\sigma_i^{\phi_s} = \cos \phi_s \sigma_i^x + \sin \phi_s \sigma_i^y$, where the spin-phase is $\phi_s = \frac{\phi_b + \phi_r + \pi}{2}$ and the motional-phase is $\phi_M = \frac{\phi_b - \phi_r}{2}$ for the phase-sensitive realization of the MS scheme⁴⁹. The unitary time evolution operator under this Hamiltonian ($U(t) = e^{-iHt}$) can be found by taking the Magnus expansion, which after appropriate approximation, leads to an effective Hamiltonian¹³

$$H = \sum_{i,j} J_{ij} \sigma_i^{\phi_s} \sigma_j^{\phi_s}. \quad (5)$$

In the far detuned limit ($\delta_m \gg \eta\Omega$), where the virtual couplings to the phonon modes are sufficiently suppressed, the analytical form of the

Ising coupling between ions i and j is given by¹³

$$J_{ij} = \Omega^2 \nu_R \sum_m \frac{b_{im} b_{jm}}{\mu^2 - \nu_m^2} \approx \frac{J}{|i-j|^p}, \quad (6)$$

where $\nu_R = \hbar \delta k^2 / (8\pi^2 M)$ is the recoil frequency, and b_{im} is the eigenvector matrix element of the i -th ion's participation in the m -th motional mode ($\sum_i |b_{im}|^2 = \sum_m |b_{im}|^2 = 1$), M is the mass of the single ion. J is the effective interaction strength obtained by a power-law fit of the interaction matrix elements, and $J/2\pi$ ranges within (0.25 to 0.4) kHz in the experiment for different system sizes. If we set $\phi_r = 0$, $\phi_b = \pi$, then $\phi_M = \pi/2$ and $\phi_s = \pi$, which makes the Hamiltonian of Eq. (5) an effective $\sigma^x \sigma^x$ interaction. We can change this phase by changing the input waveform to the acousto-optic-modulator. Similarly, we set $\phi_r = 0$, $\phi_b = 0$ to obtain an effective $\sigma^x \sigma^y$ interaction. In the double quench experiment, we switch these waveform phases to switch between interactions along different Bloch sphere directions.

We further apply a common offset of $2B^z$ to the frequencies of BSB and RSB tones which in the rotating frame of the qubit, results in an effective transverse field term $B^z \sum_i \sigma_i^z$ in the Hamiltonian of Eq. (5)¹³. The magnetic field strength B^z is chosen such that $B^z \ll \delta_m$ for the rotating frame approximation to be valid.

The approximate power law exponent can be theoretically tuned within the range $0 < p < 3$. However, in this experiment, we kept the exponent ≈ 0.89 for all the system sizes by tuning the axial trap frequency (ν_x) and motional detuning (μ). We also note that the experimental interaction matrix deviates from a pure power-law decay to an exponential decay at large distances, especially for large system sizes (SI Sec. VIII). In principle, one can tune this exponent by changing only the detuning (μ) (see Eq. (6)), but changing the axial trap frequency (ν_x) for different system sizes results in more self-consistent scaling of the exact spin-spin coupling matrix⁵⁰. We remark that maintaining a self-similar interaction matrix can also be achieved with individual optical control over all the ions⁵¹, but it is beyond the scope of this experimental setup, which features global optical control.

Experimental error sources

One of the main challenges in scaling up the system size is to maintain the fidelity of the quantum simulation experiments. Among various sources of decoherence in the trapped-ion platform, such as stray magnetic and electric fields, mode frequency drifts, off-resonant motional excitation, spontaneous emission, and additional spin-motion coupling that causes the evolution to depart from ideal simulation¹³. One such important source, which becomes significant in the large system size limit, is the off-resonant excitation of the motional modes causing residual spin-motion entanglement^{50,52}. In order to trap longer linear chains while maintaining the same interaction profile, we need to operate at a lower axial confinement which can become as low as ~ 200 Hz for $N=40-50$. At such low axial confinement, the trapped ions are more susceptible to electric field noise and background collisions⁵³. The conventional laser cooling methods start to become inefficient in cooling the ions to their motional ground states, and as a result, errors due to phonon evolution get introduced in the Hamiltonian evolution. To the lowest order, such an error can be modelled as an effective bit flip error during measurement⁵⁰. Additional cooling methods such as EIT (electromagnetically induced transparency) cooling⁵⁴ and sympathetic cooling⁵³ would be useful in mitigating the effects of such errors.

Another source of bit-flip error is imperfect detection. Off-resonant pumping from the detection beam limits our detection fidelity to about 98 %. When a large number of ions are trapped in a linear chain, ions near the center of the chain are closer together than the ones at the edges. A random bit-flip error can be introduced due to leakage of light from neighbouring ions, which might cause a dark ion

to appear bright and vice versa. More details about various noise sources in this apparatus can be found in previous works^{47,50,55}.

Modeling decoherence

To account for the most relevant source of experimental dissipation, we consider an effective model that incorporates bit-flip errors in the dynamics. In this model, the density matrix evolves in time under the Lindblad master equation as

$$\frac{d\rho}{dt} = -i[H, \rho] + \kappa \sum_{i=1}^N (\sigma_i^x \rho \sigma_i^x - \rho), \quad (7)$$

where the single bit-flip rate κ is chosen such that the numerically obtained net correlators $\langle C_x^2 \rangle$ best fit the experimental data. For simplicity, we have chosen the bit-flip rate to be uniform across the chain. In the simulations, we numerically calculate the dynamics under Eq. (7) using experimental Hamiltonian parameters and the best-fit value of κ/\mathcal{J} for a given B^z/\mathcal{J} . For $N=10$, we find the best fit at $B^z/\mathcal{J} = [0.21, 0.50, 0.87, 1.00, 1.50, 1.93]$ to be $\kappa/\mathcal{J} = [0.057, 0.036, 0.089, 0.085, 0.067, 0.045]$, respectively. For $N=15$, and $B^z/\mathcal{J}=1$, we have $\kappa/\mathcal{J}=0.024$. In Supplementary Fig. 1, we present the experimentally observed dynamics (represented by dots) of the net correlator after a single quench along with their numerical simulation (represented by solid lines) with 10 and 15 ions. In the subfigure a (10 ions), different colors indicate different values of the quench parameter B^z/\mathcal{J} . In subfigure b, we show the quench to $B^z/\mathcal{J}=1$ for $N=10$ and 15. As shown in Supplementary Fig. 1, the numerical simulations show good agreement with the experimental data, capturing the damping rate as well as the frequency of the underdamped oscillations. The numerical results for 10 ions are obtained under the exact time evolution of the Lindblad master equation using QuTiP's implementation⁵⁶. Simulations for systems with 15 ions are obtained using the Monte Carlo wave function method⁵⁷. This method can, in principle, be used to simulate larger system sizes. However, optimizing the decoherence rate in order to fit the experimental data requires a large number of these simulations, thus limiting our ability to simulate larger system sizes.

Jackknife error estimation

In the experiments reported in this work, we repeat the experiment and measurement sequence 400 times to reduce the quantum projection noise. To estimate the standard errors of the two-body correlators, we have implemented a Jackknife resampling technique⁵⁸. In this method, we construct a distribution of net correlators by randomly sampling 399 experimental runs, each time leaving out only one run. We then calculate the variance of the distribution, which corresponds to the standard error of the net correlator.

Data availability

All key experimental data supporting the findings of this study are provided in the main text and Methods. The raw datasets are available from the corresponding authors upon request for purposes of academic replication and review. Access is limited due to the large size and specialized formatting of the data, which requires additional processing to ensure correct interpretation.

Code availability

The code used for analyses is available from the corresponding author upon request.

References

- Heyl, M., Polkovnikov, A. & Kehrein, S. Dynamical quantum phase transitions in the transverse-field Ising model. *Phys. Rev. Lett.* **110**, 135704 (2013).

2. Heyl, M. Dynamical quantum phase transitions: a brief survey. *EPL* **125**, 26601 (2019).
3. Marino, J., Eckstein, M., Foster, M. M. & Rey, A.M. Dynamical phase transitions in the collisionless pre-thermal states of isolated quantum systems: theory and experiments. *Rep. Progress Phys.* **85**, 116001 (2022).
4. Li, B. W. et al. Probing critical behavior of long-range transverse-field Ising model through quantum Kibble-Zurek mechanism. *arXiv:2208.03060*, (2022).
5. Jurcevic, P. et al. Direct observation of dynamical quantum phase transitions in an interacting many-body system. *Phys. Rev. Lett.* **119**, 080501 (2017).
6. Zhang, J. et al. Observation of a many-body dynamical phase transition with a 53-qubit quantum simulator. *Nature* **551**, 601–604 (2017).
7. Calabrese, P., Essler, F. H. L. & Fagotti, M. Quantum Quench in the Transverse-Field Ising Chain. *Phys. Rev. Lett.* **106**, 227203 (2011).
8. Sachdev, S. *Quantum Phase Transitions*. 2 edition (Cambridge University Press, 2011).
9. Titum, P. & Maghrebi, M. F. Nonequilibrium criticality in quench dynamics of long-range spin models. *Phys. Rev. Lett.* **125**, 040602 (2020).
10. Stankovski, T., Pereira, T., McClintock, P. V. E. & Stefanovska, A. Coupling functions: Universal insights into dynamical interaction mechanisms. *Rev. Mod. Phys.* **89**, 045001 (2017).
11. Li, H. et al. Determining the nonequilibrium criticality of a Gardner transition via a hybrid study of molecular simulations and machine learning. *Proc. Natl Acad. Sci. Usa*. **118**, e2017392118 (2021).
12. Zurek, W. H. Cosmological experiments in condensed matter systems. *Phys. Rep.* **276**, 177–221 (1996).
13. Monroe, C. et al. Programmable quantum simulations of spin systems with trapped ions. *Rev. Mod. Phys.* **93**, 025001 (2021).
14. Blatt, R. & Roos, C. F. Quantum simulations with trapped ions. *Nat. Phys.* **8**, 277–284 (2012).
15. Schreiber, M. et al. Observation of many-body localization of interacting fermions in a quasirandom optical lattice. *Science* **349**, 842–845 (2015).
16. Bernien, H. et al. Probing many-body dynamics on a 51-atom quantum simulator. *Nature* **551**, 579–584 (2017).
17. Choi, S. et al. Observation of discrete time-crystalline order in a disordered dipolar many-body system. *Nature* **543**, 221–225 (2017).
18. Wallraff, A. et al. Strong coupling of a single photon to a superconducting qubit using circuit quantum electrodynamics. *Nature* **431**, 162–167 (2004).
19. Xu, K. et al. Probing dynamical phase transitions with a superconducting quantum simulator. *Sci. Adv.* **6**, eaba4935 (2020).
20. Chang, D. E., Douglas, J. S., González-Tudela, A., Hung, C.-L. & Kimble, J. H. Colloquium: quantum matter built from nanoscopic lattices of atoms and photons. *Rev. Mod. Phys.* **90**, 031002 (2018).
21. Ye, J., Kimble, J. H. & Katori, H. Quantum state engineering and precision metrology using state-insensitive light traps. *Science* **320**, 1734–1738 (2008).
22. Raimond, J. M., Brune, M. & Haroche, S. Manipulating quantum entanglement with atoms and photons in a cavity. *Rev. Mod. Phys.* **73**, 565–582 (2001).
23. Gring, M. et al. Relaxation and prethermalization in an isolated quantum system. *Science* **337**, 1318–1322 (2012).
24. Neyenhuis, B. et al. Observation of prethermalization in long-range interacting spin chains. *Sci. Adv.* **3**, e1700672 (2017).
25. Smith, J. et al. Many-body localization in a quantum simulator with programmable random disorder. *Nat. Phys.* **12**, 907–911 (2016).
26. Choi, J. Y. et al. Exploring the many-body localization transition in two dimensions. *Science* **352**, 1547–1552 (2016).
27. Zhang, J. et al. Observation of a discrete time crystal. *Nature* **543**, 217–220 (2017).
28. Eigen, C. et al. Universal prethermal dynamics of Bose gases quenched to unitarity. *Nature* **563**, 221–224 (2018).
29. Erne, S., Buecker, R., Gasenzer, T., Berges, J. & Schmiedmayer, J. Observation of universal dynamics in an isolated one-dimensional Bose gas far from equilibrium. *Nature* **563**, 225–229 (2018).
30. Prüfer, M. et al. Observation of universal dynamics in a spinor Bose gas far from equilibrium. *Nature* **563**, 217–220 (2018).
31. García-Orozco, A. D. et al. Universal dynamics of a turbulent superfluid Bose gas. *Phys. Rev. A* **106**, 023314 (2022).
32. Huh, S. et al. Universality class of a spinor Bose–Einstein condensate far from equilibrium. *Nat. Phys.* **20**, 402–408 (2024).
33. Polkovnikov, A., Sengupta, K., Silva, A. & Vengalattore, M. Colloquium: nonequilibrium dynamics of closed interacting quantum systems. *Rev. Mod. Phys.* **83**, 863–883 (2011).
34. Giamarchi, T., Millis, A. J., Parcollet, O., Saleur, H. and Cugliandolo, L. F. *Strongly Interacting Quantum Systems out of Equilibrium: Lecture Notes of the Les Houches Summer School*. vol. 99. (Oxford University Press, 2016).
35. Mitra, A. Quantum quench dynamics. *Annu. Rev. Condens. Matter Phys.* **9**, 245–259 (2018).
36. Cazalilla, M. A. & Chung, M. Quantum quenches in the Luttinger model and its close relatives. *J. Stat. Mech. Theory Exp.* **2016**, 064004 (2016).
37. Chiocchetta, A., Gambassi, A., Diehl, S. & Marino, J. Dynamical crossovers in prethermal critical states. *Phys. Rev. Lett.* **118**, 135701 (2017).
38. Paul, S., Titum, P. & Maghrebi, M. Hidden quantum criticality and entanglement in quench dynamics. *Phys. Rev. Res.* **6**, L032003 (2024).
39. Kac, M. & Thompson, C. J. Critical behavior of several lattice models with long range interaction. *J. Math. Phys.* **10**, 1373–1386 (1969).
40. Olmschenk, S. et al. Manipulation and detection of a trapped Yb^+ hyperfine qubit. *Phys. Rev. A* **76**, 052314 (2007).
41. Cardy, J. *Scaling and renormalization in statistical physics*, volume 5. (Cambridge University Press, 1996).
42. Halimeh, J. C. et al. Prethermalization and persistent order in the absence of a thermal phase transition. *Phys. Rev. B* **95**, 024302 (2017).
43. Žunkovič, B., Heyl, M., Knap, M. & Silva, A. Dynamical quantum phase transitions in spin chains with long-range interactions: merging different concepts of nonequilibrium criticality. *Phys. Rev. Lett.* **120**, 130601 (2018).
44. Mori, T. Prethermalization in the transverse-field Ising chain with long-range interactions. *J. Phys. A: Math. Theor.* **52**, 054001 (2019).
45. An, S. et al. Experimental test of the quantum Jarzynski equality with a trapped-ion system. *Nat. Phys.* **11**, 193–199 (2015).
46. Deslauriers, L. et al. Zero-point cooling and low heating of trapped $^{111}\text{Cd}^+$ ions. *Phys. Rev. A* **70**, 043408 (2004).
47. Kim, K. et al. Entanglement and tunable spin-spin couplings between trapped ions using multiple transverse modes. *Phys. Rev. Lett.* **103**, 120502 (2009).
48. Mølmer, K. & Sørensen, A. Multiparticle entanglement of hot trapped ions. *Phys. Rev. Lett.* **82**, 1835–1838 (1999).
49. Inlek, I. V., Vittorini, G., Hucul, D., Crocker, C. & Monroe, C. Quantum gates with phase stability over space and time. *Phys. Rev. A* **90**, 042316 (2014).
50. Pagano, G. et al. Quantum approximate optimization of the long-range Ising model with a trapped-ion quantum simulator. *Proc. Natl. Acad. Sci. USA* **117**, 25396–25401 (2020).
51. Feng, L. et al. Continuous symmetry breaking in a trapped-ion spin chain. *Nature* **623**, 713–717 (2023).
52. Tan, W. L. et al. Domain-wall confinement and dynamics in a quantum simulator. *Nat. Phys.* **17**, 742–747 (2021).
53. Cetina, M. et al. Control of transverse motion for quantum gates on individually addressed atomic qubits. *PRX Quantum* **3**, 010334 (2022).

54. Feng, L. et al. Efficient ground-state cooling of large trapped-ion chains with an electromagnetically-induced-transparency tripod scheme. *Phys. Rev. Lett.* **125**, 053001 (2020).
55. Morong, W. et al. Engineering dynamically decoupled quantum simulations with trapped ions. *PRX Quantum* **4**, 010334 (2023).
56. Johansson, J. R., Nation, P. D. & Nori, F. Qutip: an open-source Python framework for the dynamics of open quantum systems. *Comput. Phys. Commun.* **183**, 1760–1772 (2012).
57. Mølmer, K., Castin, Y. & Dalibard, J. Monte carlo wave-function method in quantum optics. *J. Opt. Soc. Am. B* **10**, 524–538 (1993).
58. Miller, R. G. The Jackknife—a review. *Biometrika* **61**, 1–15 (1974).

Acknowledgements

We acknowledge insightful discussions with W.L. Tan and L. Feng. This material is based upon work supported by the U.S. Department of Energy (DOE), Office of Science, National Quantum Information Science Research Centers, Quantum Systems Accelerator. Additional support is acknowledged from the NSF STAQ Program (PHY-1818914), the NSF QLCI (award No. OMA-2120757), and the AFOSR MURI on Dissipation Engineering in Open Quantum Systems (FA9550-19-1-0399). M.A., D.P. and M.M. are supported by the AFOSR (FA9550-20-1-0073) and the NSF CAREER Award through DMR-2142866. P.T. acknowledges funding from DOE ASCR (ERKJ347). P.C. was supported by the Department of Defense (DoD) through the National Defense Science and Engineering Graduate (NDSEG) Fellowship Program. G.P. acknowledges that this material is based upon work supported by the U.S Department of Energy, Office of Science, Office of Nuclear Physics under the Early Career Award No. DE-SC0023806.

Author contributions

A.D., W.M., K.C., and C.M. contributed to the experimental design, construction, data collection and analysis. G.P. provided experimental support. P.C., M.A., D.P., P.T., A.V.G., and M.M. carried out the theoretical analysis. All authors contributed to the discussion of the results and the manuscript.

Competing interests

The authors declare no competing interests.

Additional information

Supplementary information The online version contains supplementary material available at <https://doi.org/10.1038/s41467-025-63398-y>.

Correspondence and requests for materials should be addressed to Arinjoy De.

Peer review information *Nature Communications* thanks Christian Schmiegelow and the other anonymous reviewer(s) for their contribution to the peer review of this work. A peer review file is available.

Reprints and permissions information is available at <http://www.nature.com/reprints>

Publisher's note Springer Nature remains neutral with regard to jurisdictional claims in published maps and institutional affiliations.

Open Access This article is licensed under a Creative Commons Attribution-NonCommercial-NoDerivatives 4.0 International License, which permits any non-commercial use, sharing, distribution and reproduction in any medium or format, as long as you give appropriate credit to the original author(s) and the source, provide a link to the Creative Commons licence, and indicate if you modified the licensed material. You do not have permission under this licence to share adapted material derived from this article or parts of it. The images or other third party material in this article are included in the article's Creative Commons licence, unless indicated otherwise in a credit line to the material. If material is not included in the article's Creative Commons licence and your intended use is not permitted by statutory regulation or exceeds the permitted use, you will need to obtain permission directly from the copyright holder. To view a copy of this licence, visit <http://creativecommons.org/licenses/by-nc-nd/4.0/>.

© The Author(s) 2025